IOPscience iopscience.iop.org

Home Search Collections Journals About Contact us My IOPscience

Plasma Spray-PVD: Plasma Characteristics and Impact on Coating Properties

This article has been downloaded from IOPscience. Please scroll down to see the full text article.

2012 J. Phys.: Conf. Ser. 406 012005

(http://iopscience.iop.org/1742-6596/406/1/012005)

View the table of contents for this issue, or go to the journal homepage for more

Download details:
IP Address: 134.94.122.242
The article was downloaded on 28/06/2013 at 10:17

Please note that terms and conditions apply.

Journal of Physics: Conference Series **406** (2012) 012005 doi:10.1088/1742-6596/406/1/012005

# Plasma Spray-PVD: Plasma Characteristics and Impact on Coating Properties

**G Mauer and R Vaßen**

Forschungszentrum Jülich, Institute of Energy and Climate Research (IEK-1)
52425 Jülich, Germany

E-mail: g.mauer@fz-juelich.de

**Abstract**. Typical plasma characteristics of the plasma spray-physical vapour deposition (PS-PVD) process were investigated by optical emission spectroscopy. Electron temperatures were determined by Boltzmann plots while temperatures of the heavy species as well as electron densities were obtained by broadening analysis of spectral lines. The results show how the plasma properties and thermodynamic equilibrium conditions are affected by the admixture of hydrogen and the ambient chamber pressure. Some experimental examples of PS-PVD coatings demonstrate the impact on feedstock treatment and deposited microstructures.

## 1. Introduction

The very low pressure plasma spray (VLPPS) process has been developed with the aim of depositing uniform and thin coatings with large area coverage based on plasma spraying. At typical pressures below 500 Pa, the characteristics of the plasma jet change compared to conventional low pressure plasma spraying processes (LPPS, often called vacuum plasma spraying, VPS) operating at 5-20 kPa. By VLPPS, quite thin and dense ceramic coatings can be obtained for special applications like solid oxide fuel cells [1], gas separation membranes [2], and wear protection [3].

The combination of VLPPS with enhanced electrical input power has led to the development of the plasma spray-physical vapor deposition process (PS-PVD [4], initially called LPPS-TF process, TF = thin film). At appropriate parameters it is even possible to evaporate the powder feedstock material providing advanced microstructures and non-line of sight deposition e.g. of thermal barrier coatings for turbine components [5]. Since relative large deposition rates and areas can be achieved, PS-PVD has the potential to fill the gap between PVD on the one hand and conventional plasma spraying on the other hand.

To exploit the potential of such novel gas phase deposition, the plasma characteristics and their dependency on process conditions must be better understood. Besides power, spray distance and plasma flow conditions, the characteristics of the plasma gas are important parameters which are dependent particularly on its composition and chamber pressure. Thus, plasma conditions were investigated by optical emission spectroscopy. Based on the results, the distributions of plasma temperatures and electron densities were determined. Some experimental examples are given to demonstrate the impact on coating microstructures.

## 2. Experimental

Experiments were carried out on a Sulzer Metco Multicoat PS-PVD System (Sulzer Metco, Wohlen, Switzerland) which resulted from a comprehensive reconstruction of an existing conventional LPPS system. In particular, the system is equipped with an additional vacuum pumping unit, a large vacuum blower to provide sufficient pumping capacity at low pressures, enlarged cooling capacity, additional power sources, a new torch transfer system and new control units. In addition to a modified single cathode O3CP gun, which was used in this work, also the F4-VB torch as well as the three-cathode TriplexPro torch can be operated. Figure 1 shows the facility.

Published under licence by IOP Publishing Ltd

**Figure 1.** PS-PVD facility at Forschungszentrum Jülich, IEK-1.

For the experiments an agglomerated 7-8 wt.% Yttria partially stabilized zirconia powder (YSZ, Sulzer Metco M6700) was used. The grain sizes measured by laser diffraction were $d_{10}$ = 2 µm, $d_{50}$ = 8 µm, and $d_{90}$ = 18 µm. For PS-PVD operations, the powder grain sizes should be preferably small. The substrates used were polished stainless steel and were preheated by the plasma jet immediately before coating. Table 1 shows the appropriate plasma spray parameters.

**Table 1.** Plasma spray parameters.

| | **Parameter A** | **Parameter B** |
|---|---|---|
| plasma gas | Ar 35 / He 60 slpm[a] | Ar 35 / He 60 / $H_2$ 10 slpm[a] |
| current | 2600 A | 2200 A |
| net power | 60 kW | 60 kW |
| pressure | 200-1000 Pa (varied) | 200-1000 Pa (varied) |
| powder feed rate | 1-20 g $min^{-1}$ (varied) | 1-20 g $min^{-1}$ (varied) |
| spray distance | 300-1400 mm (varied) | 300-1400 mm (varied) |

[a] slpm = standard liters per minute

The spectrometer applied for plasma characterization was an ARYELLE 200 (Laser Technik Berlin (LTB), Berlin, Germany) scanning a wavelength range of 381-786 nm. Plasma radiation was collected through a borosilicate glass window and an achromatic lens, transferred by an optical fiber to the 50 µm entrance slit and detected by a 1024x1024 CCD array. The system is equipped with an echelle grating and the spectral resolution obtained is 15.9-31.8 pm. Calibration was carried out with a spectral Hg lamp.

## 3. Plasma Characterization

Plasma characteristics were investigated by optical emission spectroscopy. Electron and excitation temperatures were determined by the Boltzmann plot method, respectively. Electron densities and heavy particle temperatures were calculated by peak broadening analysis. Some initial results based on

the first two hydrogen spectral lines of the Balmer series $H_\alpha$ and $H_\beta$ obtained at VLPPS conditions are given in [6, 7].

As the plasma jets are optically thin, the measurement is spatially integrated along the line of sight of the optical sampling setup [8]. To obtain the central characteristics of the plasma jet, generally a deconvolution of the measured two-dimensional projections of the integrated intensities must be performed to reconstruct the spatial plasma temperature field. This can be done by Abel inversion based on the assumption of axial symmetry [9]. However this method is very laborious and potentially increases the measurement errors due to high error transfer coefficients. Thus, alternative methods have also been developed to circumvent Abel inversion. In this work, a method proposed in [10] was applied to the evaluation of Boltzmann plots. However, the corrections of the temperatures obtained along the plasma jet axis were found to be small compared to the temperature bandwidths due to the standard errors of the linear fits. Hence, the uncorrected excitation temperatures were considered to be representative of the jet center zone. In contrast, a method to correct the spectral line broadening [11] yielded substantial corrections of the measured values und was thus applied for broadening analysis.

### 3.1. Boltzmann plot method

Based on spectroscopically measured emissions, plasma excitation temperatures can be determined by the atomic Boltzmann plot method [12, 13]. Applying the Boltzmann distribution, the absolute intensity $I_{jk}$ of a spectral line emitted by the plasma due to the transition from an excited state $j$ to a lower energy state $k$ is

$$I_{jk} = \frac{L h c}{4\pi \lambda_{jk}} A_{jk}\, n \frac{g_j}{Z}\; e^{\left(-E_j / k_B T_{exc}\right)} \tag{1}$$

where $L$ is the emission source depth, $h$ is the Planck constant, $c$ is the velocity of light, $A_{jk}$ is the transition probability, $n$ is the density of emitting atoms/ions, $g_j$ is the statistical weight (degeneracy) of the excited level $j$, $\lambda_{jk}$ the wavelength of the emission, $Z$ is the partition function, $E_j$ the energy of the excited level, $k_B$ the Boltzmann constant, and $T_{exc}$ the excitation temperature. If the intensities of a set of emission lines of the same final state are measured a linear plot

$$\ln\left(\frac{I_{jk}\lambda_{jk}}{g_j A_{jk}}\right) = \frac{-E_j}{k_B T_{exc}} + C, \quad C = \ln\left(\frac{L h c n}{4\pi Z}\right) \tag{2}$$

will yield a slope that is inversely proportional to the desired excitation temperature $T_{exc}$. The left side of this equation is called atomic-state distribution function (ASDF). The values of the energy of the excited level $E_j$, of the transition probability $A_{jk}$ and the statistical weight $g_j$ were taken from [14]. The intensity values were obtained from the areas under Voigt fits of the measured spectral emission line profiles. Error bars related to the temperature results were calculated based on the standard errors of the linear fits. They were found to be approximately ±5%. More details on the application of the Boltzmann plot method can be found elsewhere [15].

Thermodynamic equilibrium (TE) conditions affect the applicability of the Boltzmann plot method considerably. There are four types of balance mechanisms resulting in four corresponding distribution functions for particles and photons [16],

- Kinetic energy exchange and conservation (Maxwell distribution characterized by the kinetic temperature $T$)
- De-excitation and excitation (Boltzmann distribution characterized by the excitation temperature $T_{exc}$)
- Recombination and ionization (Saha distribution characterized by the Saha temperature $T_{Saha}$)
- Absorption and emission (Planck distribution characterized by the radiation temperature $T_{rad}$)

The TE requires that all these temperatures are unique which is often not fulfilled, Figure 2. The weakest form of TE departure is when part of the emitted radiation is not reabsorbed in the plasma and

escapes, but Maxwell, Boltzmann and Saha balances still can be maintained. As spatial and time-related gradients are the reason, this is called local thermodynamic equilibrium (LTE) [16]. A larger deviation from TE occurs if the kinetic energy transfer between electrons and heavy particles (atoms, ions) is no longer sufficient to balance energy evenly among them. This leads to the two-temperature (2T) model [17] with the kinetic electron temperature $T_e$ , the kinetic temperature of the heavy particles $T_h$ , and the non-equilibrium parameter $\theta = T_e/T_h$.

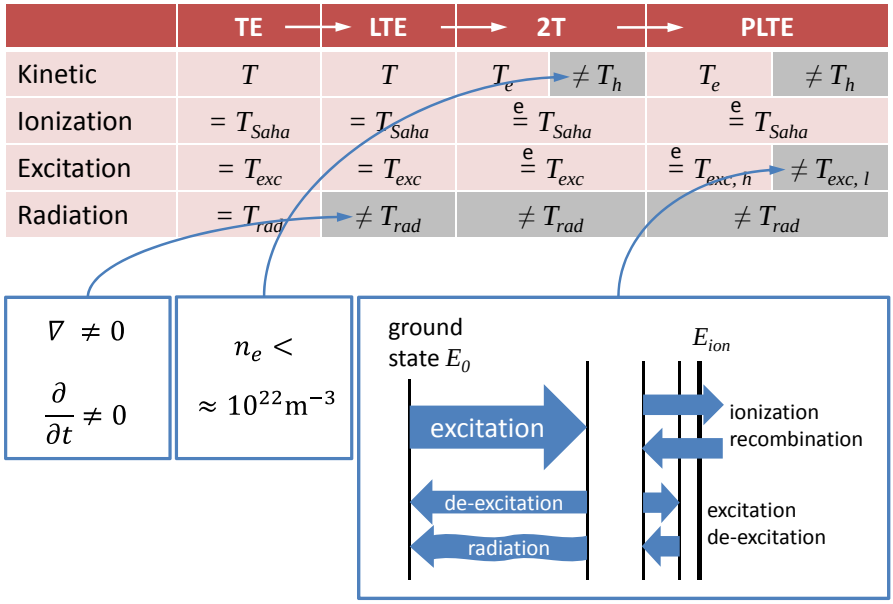


**Figure 2.** Different stages of departure from thermodynamic equilibrium in thermal plasmas; for abbreviations refer to the text.

The density distribution of excited atoms is assumed to be dominated by electron-induced transitions leading to a Boltzmann distribution where $T_{exc}$ is equal to $T_e$. Thus, the results of Boltzmann plots can be regarded to represent the electron temperatures $T_e$ [16]. Free electrons can also control the equilibrium between ionization and recombination so that $T_{Saha}$ can be identified also with $T_e$. However, atoms in the energy levels close to the ground state do not de-excite predominantly by such electron-induced transitions, but rather radiatively [17], Figure 2. In case of recombining plasmas as given in expanding plasma jets, this leads to underpopulation of the lower energy levels and thus to lower values of the ASDF. This situation is referred to as partial local thermodynamic equilibrium (PLTE) [18]. As a consequence, the data points of the Boltzmann plots do not develop linearly [19] and only those at higher energy levels represent $T_e$.

Figure 3 gives an example of Boltzmann plot for recombining plasmas. Fifteen Ar I lines between 549.59 nm and 751.47 nm were evaluated. Four of them correspond to lower energy levels (4p – 4s). It is evident that they are not aligned linearly with respect to the eleven other data points of the higher energy levels (4d, 6s, 5d, and 6d – 4p). Thus, they were not included into the linear regression. The excitation temperature derived from its slope $T_{exc,\,h}$ is 5065 +466/-394 K which represents $T_{Saha}$ and $T_e$ as shown in Figure 2. The error bandwidth results from the standard error of the slope of the linear fit.

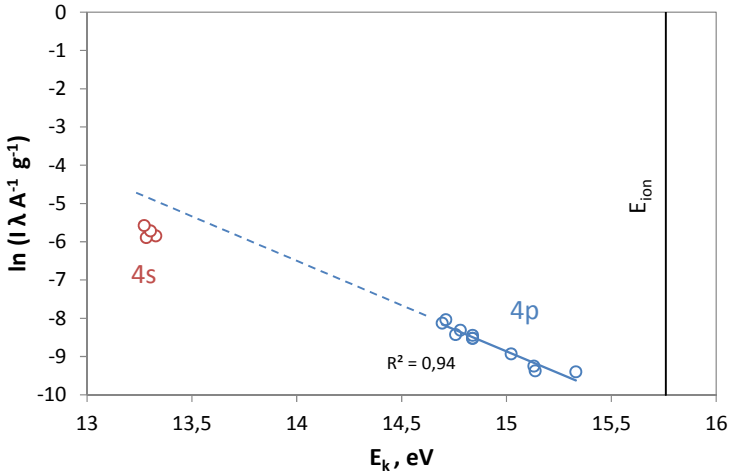


**Figure 3.** Example of Boltzmann plot for recombining plasmas with 15 evaluated Ar I spectral lines; parameter B, chamber pressure 200 Pa, and stand-off distance 400 mm.

Figure 4 gives the Boltzmann plot for the same plasma condition, but instead of Ar I lines eight He I multiplets were evaluated between 447.15 nm and 728.13 nm. For the same reasons as stated above, the data point for the transition being lowest to the ground state (3p – 2s) was not included into the linear fit since it slightly deviates. The excitation temperature obtained from the remaining seven data points (3s, 3d, 4s, and 4d - 2p) is 4344 +225/-204 K. It is not clear whether the difference to the excitation temperature obtained from the Ar I lines is substantial. However, considering He lines has practical advantage in this work since He is the largest plasma gas fraction in both investigated parameters. In particular at increasing stand-off distance the argon peaks become weak and the evaluation more uncertain.

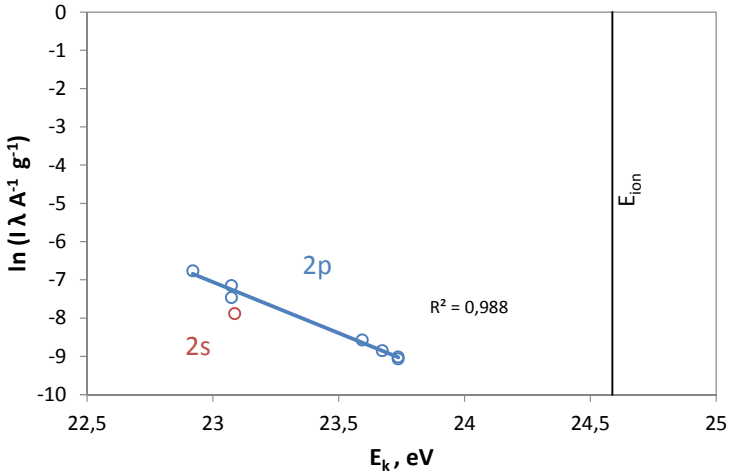


**Figure 4.** Example of Boltzmann plot for recombining plasmas with 8 evaluated He I spectral lines; parameter B, chamber pressure 200 Pa, and stand-off distance 400 mm.

### 3.2. Line broadening analysis

Spectral line broadening analysis was used to determine the electron density $n_e$ as well as the kinetic temperature of the heavy species (atoms and ions) $T_h$. In principle, several broadening mechanisms exist [20],

- Stark broadening $\Delta\lambda_S$ due to collisions between charged particles with exited emitting atoms is significant in plasmas with $n_e > 10^{21}$ m$^{-3}$. At lower electron densities, lines of non-hydrogenic species are too narrow. Hydrogen lines are subjected to linear Stark effect whereas non-hydrogenic lines show quadratic Stark effect. For neutral atom lines, electron-impact broadening produces a symmetrical, shifted profile of the Lorentzian type, while ion-contribution introduces asymmetry as well as additional contribution to the width and the shift of the profile.
- Van der Waals broadening is produced by the collisions of neutral ground state atoms and exited emitting atoms. It is usually small and can be neglected for the conditions investigated here.
- Natural broadening arises from uncertainty in energy of the states involved in the transitions. It is rarely significant in atomic spectroscopy.
- Resonance broadening is confined to lines involving an energy level being coupled to the ground state which is not relevant for the lines investigated in this work.
- Doppler broadening $\Delta\lambda_D$ occurs due to the thermal motion of excited atoms. The line intensity distribution is Gaussian.
- The line shapes obtained by a spectrometer are usually approximately Gaussian profiles. Such instrument broadening $\Delta\lambda_I$ has to be determined by means of a laser source or spectral lamp.

Those effects which give rise to Gaussian line shapes tend to be independent from those producing Lorentzian broadening profiles. As such, the convolution of these two types of functions results in the Voigt function where the Gauss contribution determines the profile core while the Lorentzian part governs the far wings. In order to separate the Gauss and Lorentz contributions, a form of the Voigt function was used where the Gaussian and the Laurentzian half widths at full maximum (HWHM) $\Delta\lambda_G/2$ and $\Delta\lambda_L/2$ are direct parameters ($\Delta\lambda_G$ and $\Delta\lambda_L$ are the full widths at half maximum, FWHM);

$$I = \frac{a_0 a_3}{2\pi\sqrt{\pi}a_2^2}\int_{-\infty}^{\infty}\frac{e^{\left(-t^2\right)}}{\frac{a_3^2}{2a_2^2}+\left(\frac{x-a_1}{\sqrt{2}a_2}-t\right)^2}dt \tag{3}$$

where $a_0$ is the area, $a_1$ the centre wavelength, $a_2$ the Gaussian half width, and $a_3$ the Lorentzian half width. Thus, the fit of the measured intensity distribution yields immediately the Lorentzian as well as the Gaussian broadening FWHMs and analogically their standard errors by

$$\Delta\lambda_G = 2a_2\sqrt{2\ln(2)},\ \Delta\lambda_L = 2a_3 \tag{4}$$

To obtain the Doppler broadening the instrument broadening has to be subtracted by

$$\Delta\lambda_D = \sqrt{\Delta\lambda_G^2 - \Delta\lambda_I^2} \tag{5}$$

Since only Stark broadening causes a significant Lorentzian contribution they can be equated

$$\Delta\lambda_S = \Delta\lambda_L \tag{6}$$

The selection of the spectral lines for broadening analysis has to be done carefully. The most widely used for diagnosis purposes because of its great Stark width is the $H_\beta$ line of the Balmer series of hydrogen at 486.13 nm [21]. It is relatively isolated, does not show significant self-absorption, and is almost independent on $T_e$ and ion dynamics effects. The latter cannot be neglected if using other species like He I [22]. There are also some well investigated Ar I lines, e. g. at 696.54 nm [23, 24, 25]. However in this work, broadening analysis was only successful using the $H_\beta$ line as it is supported by sufficient measured data points so that the Gaussian and Lorentzian broadening contributions could be separated reliably. Several non-hydrogenic lines of Ar I and He I were tried but found to be too narrow

with respect to the spectrometer resolution. Thus, the determination of $T_h$ and $n_e$ could be performed only for the hydrogen containing parameter B.

Figure 5 shows three examples of Voigt fits and residuals of the $H_\beta$ line profile at Parameter B and 400 mm stand-off distance. The quality of the fits is very similar for the three investigated chamber pressures 200, 500, and 1000 Pa. The coefficients of determination are better than 0.999 each. The developments of the residuals do not show any significant indication of asymmetry. The central dip is hardly discernible from the observed data.

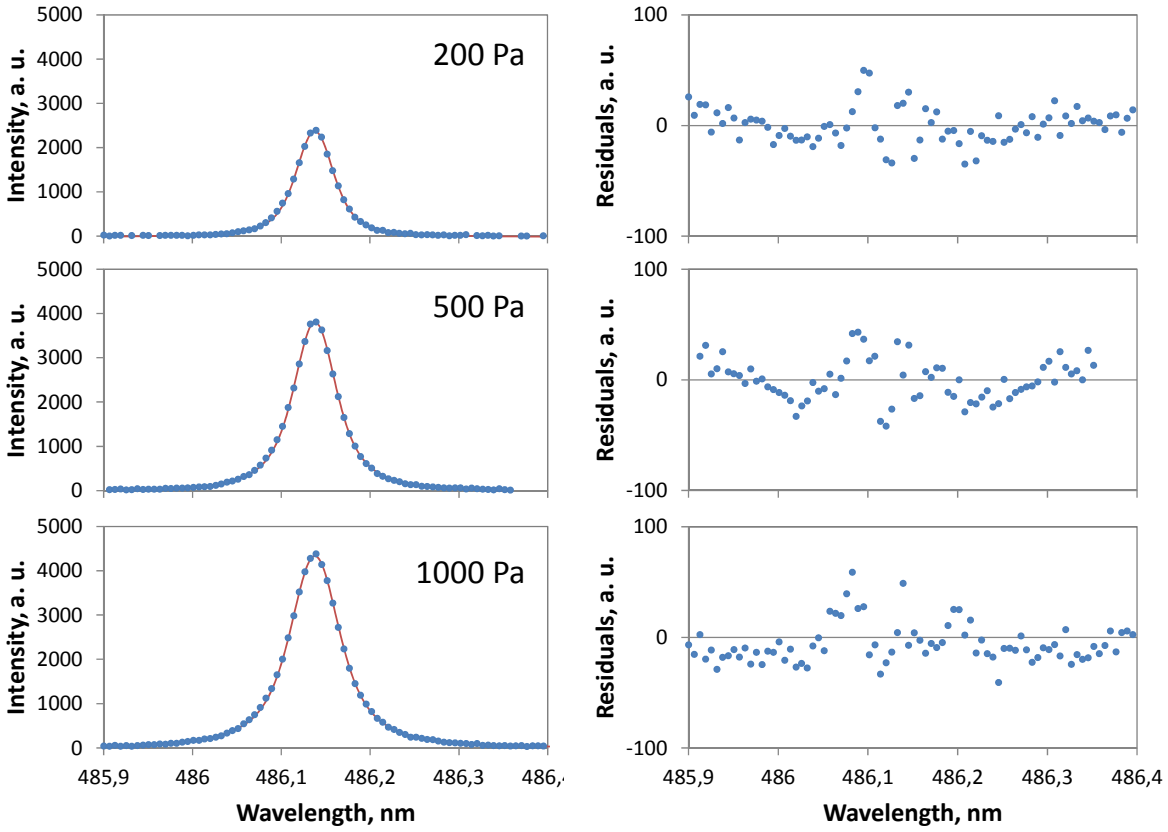


**Figure 5.** Voigt fits and residuals of $H_\beta$ line at Parameter B and 400 mm stand-off distance, chamber pressures 200, 500, and 1000 Pa.

Electron density $n_e$ (in $m^{-3}$) is calculated according to the Stark profile calculations in [26]. The method is independent of the assumption of PLTE. The FWHM (in nm) is calculated by

$$\Delta\lambda_S = 2.507 \cdot 10^{-4} \alpha \, n_e^{2/3} \tag{7}$$

The Stark broadening parameter $\alpha$ is tabulated depending on $n_e$ and $T_e$; the latter dependence is only weak. Based on the Lorentzian broadening contribution separated from the measured broadening as described above, equation 6 was solved iteratively for $n_e$. Cross checks with other simplified approaches [27, 28] yielded similar results. Error bandwidths related to the electron density results were checked based on the standard errors of the Voigt fits. They were found to be small by approximately ±5% und hence not included in the graphs.

The FWHM due to Doppler broadening is calculated according to [29] by

$$\Delta\lambda_D = 2\lambda_0 \left(\frac{2k_B T_h \ln(2)}{M\,u\,c^2}\right)^{1/2} \tag{8}$$

where $\lambda_0$ is the central wavelength of the emission line, $k_B$ is the Boltzmann constant, $M$ is the relative atomic mass of the absorbing atom, $u$ is the atomic mass unit, and $c$ is the speed of light. Based on the Gaussian broadening contribution separated from the measured broadening and corrected for the instrumental broadening as described above, equation 7 was solved for $T_h$. Error bars related to the temperature results were calculated based on the standard errors of the linear fits. They were found to be approximately ±10 to 15%. Thus, the temperature determination based on Doppler broadening turned out to be prone to uncertainties.

The investigated plasma jets are supersonic when they exit the nozzle. The first transition to subsonic conditions is indicated by the so-called Mach disk. Further downstream, expansion and compression zones due to reflections at the jet fringes can be observed in particular at higher chamber pressures. In addition, the turbulent zones at the jet ends move closer to the torch exit with increasing chamber pressures. Thus, local pressure differences compared to the chamber pressure occur. However, these local static pressures $p_{stat}$ were not determined. Hence, only for the relatively homogeneous jet at the lowest chamber pressure of 200 Pa but not for 500 Pa and 1000 Pa the neutral densities $n_0$ and the ionization degrees $x_{ion}$ were determined assuming that the pressure at the measurement positions in the jet was equal to the chamber pressure by

$$n_0 = \left(\frac{p_{stat}}{k_B} - n_e(T_h + T_e)\right) T_h^{-1} \tag{9}$$

(only single ionization is considered). $x_{ion}$ is then obtained by

$$x_{ion} = n_e/(n_o + n_e) \tag{10}$$

## 4. Results and Discussion

### 4.1. Electron temperatures

The results of the determination of the electron temperatures are given in Figure 6 for parameters A and B in dependence on the stand-off distance and the chamber pressure. For the hydrogen containing parameter B the values are on a lower level than for parameter A with He and Ar only. For both parameters the net power was the same. But the addition of almost 10% hydrogen for parameter B consumes energy for heating and dissociation. Furthermore the jet is broadened and the radial temperature profile is probably flattened. This is supposed to be the explanation for the lower temperature level.

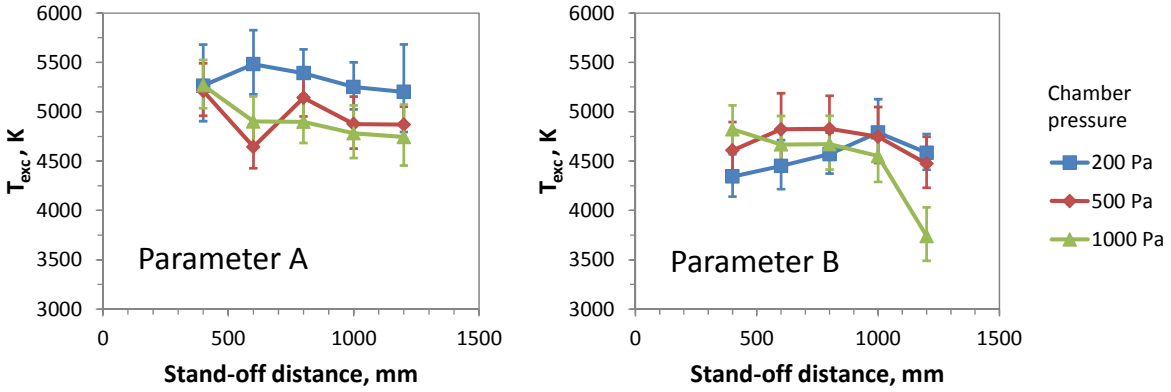


**Figure 6.** Electron temperatures determined for parameters A and B in dependence on the stand-off distance and the chamber pressure; the error bars result from the standard errors of the linear fit slopes of the Boltzmann plots.

For parameter B, the electron temperatures generally decrease with larger stand-off distances; only at 200 Pa and 500 Pa the densities increase initially. It is assumed that dissociation energy of

recombining hydrogen atoms is released and transferred [30]. At 1000 Pa, this happens closer to the nozzle so that it was not covered by the measurements. At higher chamber pressures, the electron densities are slightly affected probably by the formation of expansion and compression zones due to the equilibration of the static pressure in the jet and the ambient pressure.

4.2. Electron densities and ionization rates

Electron densities and ionization rates determined for parameter B are given in Figure 7 in dependence on the stand-off distance and the chamber pressure. In principle, the electron densities decrease along the jet axis due to recombination and thus the ionization rate drops. The decrease is faster if the jet becomes shorter at higher chamber pressures of 500 Pa and 1000 Pa. Here, the electron densities are larger as the density in the jet is higher in general. The initial increase of the electron densities is assumed to be associated to static pressure and temperature alterations along the jet axis due to equilibration with the ambient pressure [30]. As recombination is already advanced at the applied measurement positions, the ionization rates are on low level. This is confirmed by the fact that no significant ionic lines of Ar II or He II are observed in the measured spectra.

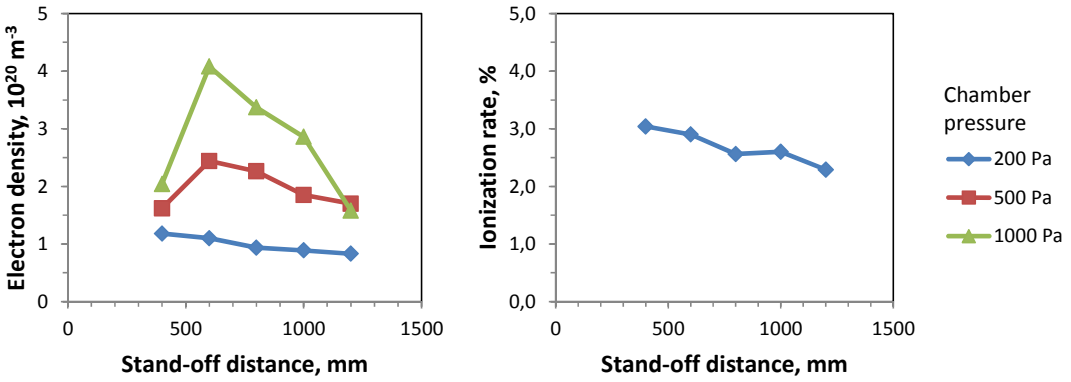


**Figure 7.** Electron densities and ionization rates determined for parameter B in dependence on the stand-off distance and the chamber pressure.

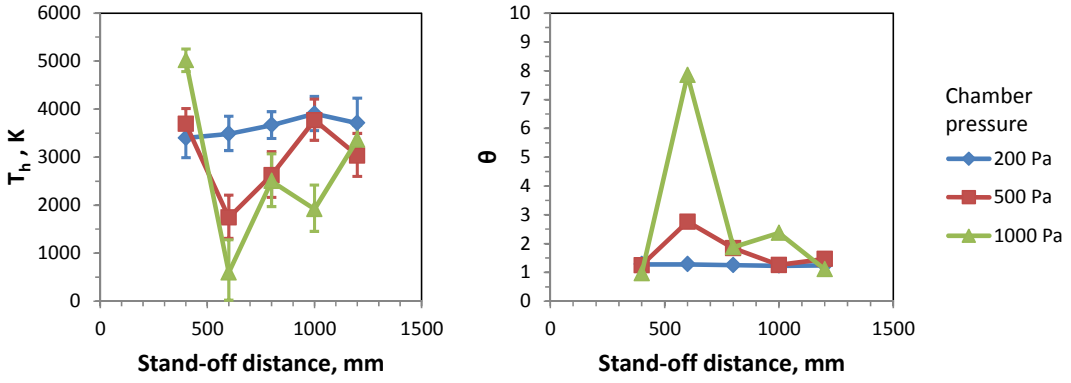


**Figure 8.** Temperatures of the heavy species and non-equilibrium parameters determined for parameter B in dependence on the stand-off distance and the chamber pressure; the error bars result from the standard errors of the Voigt fit parameters of the spectral line profile.

4.3. Temperatures of the heavy species

Temperatures of the heavy species (atoms and ions) and non-equilibrium parameters are given in Figure 8 determined for parameter B in dependence on the stand-off distance and the chamber

pressure. For the lowest pressure of 200 Pa, $T_h$ increases at larger stand-off distances in a similar manner as $T_e$ (cp. Figure 6). As for the electrons, this can be explained by the release and transfer of dissociation energy of recombining hydrogen atoms. Here, $\theta$ is not far from unity (between 1.23 and 1.28) so that the departure from LTE is not large. However, at higher chamber pressures, large alterations of $T_h$ occur due to static pressure and temperature changes along the jet axis and the formation of off-axial maxima in the expansion zones [30]. $T_e$ is distinctly less affected (cp. Figure 6) as electrons do not experience a shock and their velocity is never supersonic due to their low mass [31]. This results in considerable kinetic non-equilibria between electrons and heavy particles.

## 5. PS-PVD coating microstructures

Some experimental examples are given to demonstrate the impact of plasma characteristics on PS-PVD coating microstructures [32]. The torch was equipped with a two-fold internal powder injection. The feedstock agglomerates are defragmented into sub-micron primary particles and heated already inside the nozzle where the plasma gas density is still high before exiting. This results in the formation of molten droplets and vapor with atomic species. The supersonic conditions effect that the plasma gas can exit the nozzle at a pressure which is different from the chamber pressure. As the flow is faster than the pressure waves traveling in the fluid at the local speed of sound, no information on the chamber pressure is carried inside the nozzle [33]. In the experiments, the development of clusters was also observed showing neither atomic nor liquid-like behavior at deposition. Such clusters may be the product of an incomplete evaporation or nucleation and growth. They play an important role for the formation either of columnar or dense coating microstructures. Vapor, cluster, and droplets are then transported to the substrate interacting with the plasma flux.

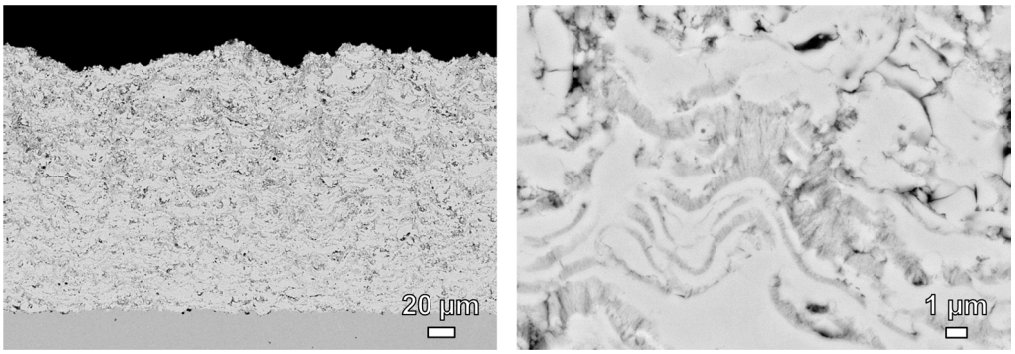


**Figure 9.** Mixed mode deposition from liquid splats, nano-sized clusters, and vapor phase; parameter B, chamber pressure 200 Pa.

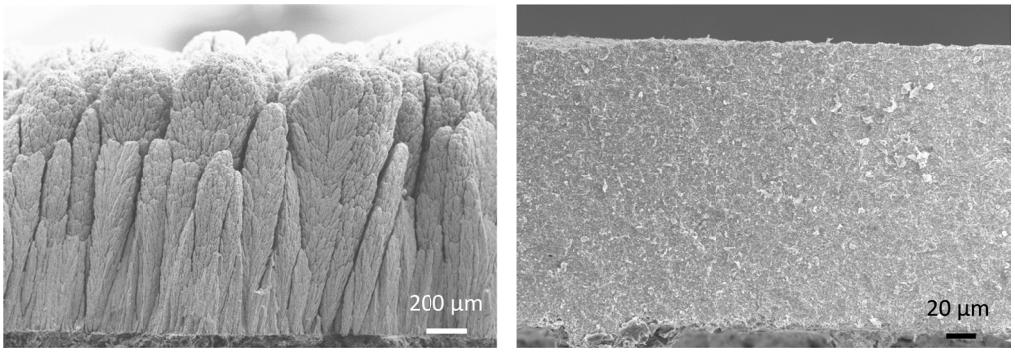


**Figure 10.** Columnar (left) and dense structured (right) coatings from nano-sized clusters and vapor phase; parameter A, chamber pressure 200 Pa.

Figure 9 gives an example of a mixed mode deposition from liquid splats, nano-sized clusters, and vapor phase obtained from parameter B [34]. Here, the addition of hydrogen broadens the plasma jet

and leads to energy consumption for dissociation. Thus, evaporation of the feedstock is incomplete. Figure 10 shows columnar and dense structured coatings only from nano-sized clusters and vapor phase obtained by parameter A [35]. The difference of these two structures is due to the plasma flow conditions along the substrate surface and shadowing effects [32].

## 6. Conclusion

The results of the optical emission spectroscopy show that the plasma jet at PS-PVD conditions consists of recombining plasma with a low degree of ionization. The admixture of hydrogen to the He/Ar plasma gas affects the plasma enthalpy due to initial consumption and later release of dissociation energy. Obviously, there is no significant effect on the transport properties. However, the hydrogen broadens the plasma jet and probably flattens the radial temperature profiles. Experimental examples show that this has impacts on the heating of the feedstock and the microstructure of the deposited coatings.

At the lowest investigated chamber pressure of 200 Pa, a moderate departure from LTE was found. Here, the distribution of temperatures and electron densities along the jet axis was smooth and homogeneous. In contrast, at higher chamber pressures large fluctuations of the plasma characteristics and thus distinct non-equilibrium conditions occur due to static pressure and temperature changes along the jet axis. Such conditions are assumed to be detrimental for treatment and transport of the feedstock. In future work this could be investigated more in detail by calculation of transport properties considering non-equilibria.

## Acknowledgements

The authors would like to acknowledge gratefully the spectral emission spectroscopic measurements by Dr. Andreas Hospach and Dr. Nikolay Zotov, Forschungszentrum Jülich, IEK-1.

## References

[1] Verdy C, Zhang C, Sokolov D, Liao H, Klein D, and Coddet C 2008 Gas-tight Coatings Produced by Very Low Pressure Plasma Spraying *Thermal Spray 2008: Thermal Spray Crossing Borders* on CD-ROM Lugscheider E Ed June 02-04, 2008 (Maastricht, The Netherlands) Verlag für Schweißen und verwandte Verfahren 2008 398-402

[2] Mauer G, Vaßen R, and Stöver D 2010 Thin and Dense Ceramic Coatings by Plasma Spraying at Very Low Pressure *J. Therm. Spray Technol.* **19** 495-501

[3] Zhu L, Zhang N, Zhang B, Sun F, Bolot R, Planche M-P, Liao H, and Coddet C 2011 Very low pressure plasma sprayed alumina and yttria-stabilized zirconia thin dense coatings using a modified transferred arc plasma torch *Appl. Surf. Sci.* **258** 1422-8

[4] von Niessen K and Gindrat M 2011 Plasma Spray-PVD: A New Thermal Spray Process to Deposit Out of the Vapor Phase *J. Therm. Spray Technol.* **20** 736-43

[5] von Niessen K, Gindrat M, and Refke A 2010 Vapor Phase Deposition Using Plasma Spray-PVD *J. Therm. Spray Technol.* **19** 502-9

[6] Zhang N, Sun F, Zhu L, Verdy C, Planche M P, Liao H, Dong C, and Coddet C 2011 Characteristics of Cu Film Deposited Using VLPPS, *J. Therm. Spray Technol.* **20** 351-7

[7] Zhang N, Sun F, Zhu L, Planche M P, Liao H, Dong C, and Coddet C 2011 Electron Temperature and Density of the Plasma Measured by Optical Emission Spectroscopy in VLPPS conditions, *J. Therm. Spray Technol.* **20** 1321-7

[8] Yugeswaran S and Selvarajan V 2009 Excitation temperature and electron number density behavior of atmospheric pressure D.C. argon plasma jet during spheroidization of nickel, *Vacuum* **83** 841-7

[9] Bockasten K 1961 Transformation of Observed Radiances into a Radial Distribution of the Emission of a Plasma, *J. Opt. Soc. Am.* **51** 943-7

[10] Kurskov A A, Ershov-Pavlov E A, and Chvyaleva L V 1986 Measurement of the local temperature in a plasma without the use of Abel inversion, *J. Appl. Spec.* **45** 1155-9

[11] Kurskov A A, Ershov-Pavlov E A, and Chvyaleva L V 1989 Determination of half-width of spectral lines of radiation of an inhomogeneous plasma, *J. Appl. Spec.* **51** 1135-8

[12] Semenov S and Cetegen B 2001 Spectroscopic Temperature Measurements in Direct Current Arc Plasma Jets Used in Thermal Spray Processing of Materials, *J. Therm. Spray Technol.* **20** 326-36

[13] Tu X, Chéron B G, Yan J H, and Cen K F 2007 Electrical and spectroscopic diagnostic of an atmospheric double arc argon plasma jet, *Plasma Sources Sci. Technol.* **16** 803-12
[14] Ralchenko Y, Kramida A, Reader J, and NIST ASD Team (2011). *NIST Atomic Spectra Database* (version 4.1), [Online]. Available: http://physics.nist.gov/asd [Friday, 15-Jun-2012 08:25:13 EDT]. National Institute of Standards and Technology, Gaithersburg, MD
[15] Mauer G, Vaßen R, and Stöver D 2011 Plasma and Particle Temperature Measurements in Thermal Spray: Approaches and Applications, *J. Therm. Spray Technol.* **20** 391-406
[16] van der Mullen J A M 1990 Excitation equilibria in plasmas; a classification, *Phys. Rep.* **191** 109-220
[17] Calzada M D, Moisan M, Gamero A, and Sola A 1996 Experimental investigation and characterization of the departure from local thermodynamic equilibrium along a surface-wave-sustained discharge at atmospheric pressure, *J. Appl. Phys.* **80** 46-55
[18] Rat V, Murphy A B, Aubreton J, Elchinger M F, and Fauchais P 2008 Treatment of non-equilibrium phenomena in thermal plasma flows, *J. Phys. D: Appl. Phys.* **41** 183001
[19] Quintero M C, Rodero A, García M C, and Sola A 1997 Determination of the Excitation Temperature in a Nonthermodynamic-Equilibrium High-Pressure Helium Microwave Plasma Torch, *Appl. Spectrosc.* **51** 778-84
[20] Konjević N 1999 Plasma Broadening and Shifting of Non-Hydrogenic Spectral Lines: Present Status and Applications, *Phys. Rep.* **316** p 339-401
[21] Gigosos M A and Cardeñoso V 1996 New plasma diagnosis tables of hydrogen Stark broadening including ion dynamics, *J. Phys. B: At. Mol. Opt. Phys.* **29** 4795-838
[22] Kelleher D E 1981 Stark broadening of visible neutral helium lines in a plasma, *J. Quant. Spectrosc. Radiat. Transfer* **25** 191-220
[23] Dong L, Ran J, and Mao Z 2005 Direct measurement of electron density in microdischarge at atmospheric pressure by Stark broadening, *Appl. Phys. Lett.* **86** 161501
[24] Pellerin S, Musiol K, Pokrzywka B, and Chapelle J 1996 Stark width of $4p'[^1/_2]$-$4s[^3/_2]^0$ Ar I transition (696.543 nm) *J. Phys. B: At. Mol. Opt. Phys.* **29** 3911-24
[25] Dimitrijević M S, Christova M, and Sahal-Bréchot S 2007 Stark broadening of visible Ar I spectral lines, *Phys. Scr.* **75** 809-19
[26] Kepple P and Griem H R 1968 Improved Stark Profile Calculations for the Hydrogen Lines $H_\alpha$, $H_\beta$, $H_\gamma$, and $H_\delta$, *Phys. Rev.* **173** 317-325
[27] Wiese W L, Kelleher D E, and Paquette D R 1972 Detailed Study of the Stark Broadening of Balmer Lines in a High-Density Plasma, *Phys. Rev. A* **6** 1132-53
[28] Balcon N, Aanesland A, and Boswell R 2007 Pulsed RF discharges, glow and filamentary mode at atmospheric pressure in argon, *Plasma Sources Sci. Technol.* **16** 217-25
[29] Griem H R *Plasma Spectroscopy*, McGraw-Hill, New York 1964
[30] Selezneva S E, Sember V, Gravelle D V, and Boulos M I 2002 Spectroscopic validation of the supersonic plasma jet model, *J. Phys. D: Appl. Phys.* **35** 1338-49
[31] Sember V, Gravelle D V, and Boulos M I 2002 Spectroscopic study of a supersonic jet generated by an ICP torch with a convergent-divergent nozzle, *J. Phys. D: Appl. Phys.* **35** 1350-61
[32] Mauer G, Zotov N, Hospach A, and Vaßen R 2012 Process Conditions and Microstructures of Ceramic Coatings by Gas Phase Deposition Based on Plasma Spraying, *Thermal Spray 2012: Proceedings from the International Thermal Spray Conference and Exposition*, May 21–24, 2012, Houston, Texas, USA, (Ed.) R.S. Lima, A. Agarwal, M.M. Hyland, Y.-C. Lau, C.-J. Li, A. McDonald, F.-L. Toma, ASM International, Materials Park, Ohio, USA, 2012, 828-33
[33] Jodoin B, Gindrat M, Dorier J-L, Hollenstein C, Loch M, and Barbezat G 2002 Modeling and Diagnostics of a Supersonic DC Plasma Jet Expanding at Low Pressure, *International Thermal Spray Conference*, E. Lugscheider, C.C. Berndt, Ed., March 04-06, 2002 (Essen, Germany), Verlag für Schweißen und verwandte Verfahren DVS-Verlag, 2002, 716-20
[34] Hospach A, Mauer G, Vaßen R, and Stöver D 2011 Columnar Structured Thermal Barrier Coatings (TBCs) by Thin Film Low Pressure Plasma Spraying (LPPS-TF), *J. Therm. Spray Technol.* **20** 116-20
[35] Hospach A, Mauer G, Vaßen R, and Stöver D 2012 Characteristics of Ceramic Coatings Made by Thin Film Low Pressure Plasma Spraying (LPPS-TF), *J. Therm. Spray Technol.* **21** 435-40